Delft University of Technology

Source deghosting of coarsely sampled common-receiver data using a convolutional neural network

Vrolijk, Jan Willem; Blacquière, Gerrit

Important note
To cite this publication, please use the final published version (if applicable).
Please check the document version above.

Source deghosting of coarsely sampled common-receiver data using a convolutional neural network

Jan-Willem Vrolijk[1] and Gerrit Blacquière[1]

ABSTRACT

It is well known that source deghosting can best be applied to common-receiver gathers, whereas receiver deghosting can best be applied to common-shot records. The source-ghost wavefield observed in the common-shot domain contains the imprint of the subsurface, which complicates source deghosting in the common-shot domain, in particular when the subsurface is complex. Unfortunately, the alternative, that is, the common-receiver domain, is often coarsely sampled, which complicates source deghosting in this domain as well. To solve the latter issue, we have trained a convolutional neural network to apply source deghosting in this domain. We subsample all shot records with and without the receiver-ghost wavefield to obtain the training data. Due to reciprocity, these training data are a representative data set for source deghosting in the coarse common-receiver domain. We validate the machine-learning approach on simulated data and on field data. The machine-learning approach gives a significant uplift to the simulated data compared to conventional source deghosting. The field-data results confirm that the proposed machine-learning approach can remove the source-ghost wavefield from the coarsely sampled common-receiver gathers.

INTRODUCTION

In marine seismic acquisition, sources are towed under the sea surface. Due to the large impedance contrast between water and air, the sea surface reflection coefficient is very close to -1 (more precisely, -0.99956). Therefore, at the sea surface, the upgoing part of the source wavefield becomes a downgoing wavefield, the so-called source-ghost wavefield. The same mechanism is responsible for the receiver-ghost wavefield, which is the sea surface reflection of the total upgoing wavefield. The source- and receiver-ghost wavefields cause notches in the wavenumber-frequency domain. The presence of these spectral notches, due to destructive interference, limits the usable bandwidth and interpretability of marine seismic data. This is the main reason it is desired to remove the source- and the receiver-ghost wavefield. These processes are called source and receiver deghosting. Note that multilevel and multicomponent acquisition systems (Tenghamn et al., 2007; Day et al., 2013) measure additional information to fill in the notches due to the receiver-ghost wavefield. To fill in notches due to the source-ghost wavefield, multilevel sources have been proposed as well (Hopperstad et al., 2008; Parkes and Hegna, 2011; Caporal et al., 2018).

In this paper, we focus on conventional pressure-only data acquired with a streamer and with an air-gun array acting as a single source. In this case, most receiver deghosting methods require common-shot records that are densely sampled in the inline direction. A full-3D wavefield receiver deghosting method requires densely sampled receivers in the inline and crossline directions. It is quite common that there are acquisition gaps on the source side as well as at the receiver side in marine seismic acquisition due to economic reasons, obstructions such as islands and oil rigs, unfavorable bathymetry, and environmental regulations. In practice, the acquisition gaps at the source side are often larger than at the receiver side. Large gaps in the source acquisition limit the applicability of source-deghosting methods that are best suited for densely sampled common-receiver data.

There are methodologies such as carpet shooting (Walker et al., 2014) that provide dense source sampling, but, in this paper, we focus on the effects and the implications of coarse source sampling on source deghosting. At the receiver side, multicomponent data can assist in overcoming the sampling requirement by integrating the receiver interpolation with up-down decomposition (Tang and Campman, 2017). Sun and Verschuur (2017) propose a method for pressure data at the detector side that implicitly handles sparse data. Interpolation of seismic sources with large acquisition gaps is not

[1]Delft University of Technology, Department of Geoscience, Delft 2628 CN, the Netherlands. E-mail: Jan-Willem.Vrolijk@tno.nl (corresponding author); G.Blacquiere-1@tudelft.nl.

straightforward, especially if the subsurface is complex. Nonlinear effects complicate the source deghosting as well. Parkes and Hatton (1986) describe the so-called "shot effect" that resulted in such nonlinear behavior. Ghost cavitation is another nonlinear effect that can occur near the water-air interface (Landrø et al., 2011; Khodabandeloo and Landrø, 2018). Near-field hydrophone measurements can be used to derive a far-field signature that includes the ghost effect with its nonlinearities, which can be used to estimate the source-deghosted data (Ziolkowski et al., 1986; Hampson, 2017; Kryvohuz and Campman, 2017; Telling and Grion, 2019). Source deghosting is often carried out in the common-shot domain to satisfy sampling requirements. However, when observed in the common-shot domain, the source-ghost wavefield has traveled through the earth with all of its complexity, which causes the removal of the source-ghost wavefield in this domain to be far from straightforward (Blacquière and Sertlek, 2019).

We propose a machine-learning approach to remove the source-ghost wavefield in the coarsely sampled common-receiver domain. The architecture of the network that we use in this paper is based on recently developed convolutional neural networks (CNN) in deep learning for medical image recognition (Ronneberger et al., 2015; Quan et al., 2016). These networks are applicable in the case of a limited amount of training data and are known to be effective for data that resemble the training data. Neural networks were introduced in geophysics quite some time ago, for example, in seismic inversion (Röth and Tarantola, 1994; Nath et al., 1999) and interpretation (Glinsky et al., 2001). In more recent years, the development of powerful graphics processing units has led to numerous deep-learning algorithms in seismic processing (Mikhailiuk and Faul, 2018; Sun and Demanet, 2018; Siahkoohi et al., 2019b), interpretation (Huang et al., 2017; Ross and Cole, 2017; Shi et al., 2018; Pham et al., 2019), and inversion (Lewis and Vigh, 2017; Araya-Polo et al., 2018; Das et al., 2019).

In the first part of the paper, we describe the theoretical framework of source deghosting carried out in the common-receiver domain and receiver deghosting carried out in the common-shot domain. Then, we show the limitation of source deghosting carried out in the coarsely sampled common-receiver domain. After that, we demonstrate the limitations of a source-deghosting method carried out in a densely sampled common-shot domain.

In the second part of this paper, we introduce a strategy to obtain a suitable CNN-training data set. We assume that receivers are densely sampled and sources are coarsely sampled. To ensure that the shot records resemble the receiver gathers, we first need to redatum the receivers to the source level and replace the original receiver-ghost wavefield with a receiver-ghost wavefield that corresponds to that same level, that is, the source level. After that, we subsample the receivers to mimic the coarse sampling of the sources. Now, we have input training data that consist of coarsely sampled shot records including the source- and receiver-ghost wavefields. We also prepare output training data that consist of receiver-deghosted coarsely sampled shot records. After the training, we test the network for the purpose of source deghosting of coarsely sampled receiver gathers. In the first machine learning example, we train and apply the CNN to numerical data. This example shows that we are able to train a network and obtain a significant uplift of the source-deghosted data. In the second machine learning example, we test the method on a field data set, acquired offshore Australia.

THE GHOST MODEL

As mentioned, the reflectivity at the sea surface is very close to -1. Therefore, at the source level $z_s(x, y)$, the total downgoing wavefield is the combination of the direct source wavefield and its reflection at the sea surface. The latter is the so-called source-ghost wavefield. Similarly, at the receiver level $z_d(x, y)$, the combination of the direct upgoing and reflected downgoing wavefield is measured. The latter is the so-called receiver-ghost wavefield. There are various methods to include the shape and dynamics of a rough sea surface (King and Poole, 2015; Grion et al., 2016; Vrolijk and Blacquière, 2020). However, in this paper, we neglect the shape and dynamics of the sea surface and assume that the sea surface is well represented by a horizontal sea surface z_0. We formulate a monochromatic seismic data set $\mathbf{P}$, including the receiver- and source-ghost wavefields, according to the matrix notation introduced by Berkhout (1985) as

$$\mathbf{P}(z_d; z_s) = \mathbf{D}(z_d)\mathbf{G}(z_d, z_d)\mathbf{X}(z_d, z_s)\mathbf{G}(z_s, z_s)\mathbf{S}(z_s), \quad (1)$$

where $\mathbf{S}$ describes the locations and spectral properties of the sources, $\mathbf{X}$ is the transfer function of the subsurface below the source and receiver level, $\mathbf{D}$ describes the locations and spectral properties of the receivers, and $\mathbf{G}$ is the source or the receiver ghost matrix. The source ghost matrix at the source side is given by

$$\mathbf{G}(z_s, z_s) = \mathbf{I} - \mathbf{W}(z_s, z_0)\mathbf{W}(z_0, z_s), \quad (2)$$

where $\mathbf{W}(z_0, z_s)$ describes forward propagation from the source level up to the sea surface, $\mathbf{W}(z_s, z_0)$ describes forward propagation from the sea surface down to the source level, and the minus sign represents the strong sea surface reflectivity of -1. The receiver ghost matrix is similar to the source ghost matrix, with propagation matrices corresponding to the receiver level z_d. In the case of a flat sea surface and a horizontal receiver level z_d or a horizontal source level z_s, we can replace the matrix multiplication in the space-frequency domain by a simple multiplication in the wavenumber-frequency domain with the ghost operator:

$$\tilde{G}(k_x; \omega) = 1 - e^{-2jk_z \Delta z}, \quad (3)$$

where k_z is the vertical component of the wave vector. In the case of ideal spatial receiver sampling, that is, sampling according to the Nyquist criterion and unit receivers, the detector matrix becomes a unity matrix, that is, $\mathbf{D}(z_d) = \mathbf{I}$, and the right side of equation 1 becomes the following matrix product:

$$\mathbf{G}(z_d, z_d)\mathbf{X}(z_d, z_s)\mathbf{G}(z_s, z_s)\mathbf{S}(z_s). \quad (4)$$

A shot record representation of this matrix product is given by column vector

$$\mathbf{G}(z_d, z_d)\mathbf{X}(z_d, z_s)\mathbf{G}(z_s, z_s)\vec{S}(z_s). \quad (5)$$

Applying the inverse of $\mathbf{G}(z_d, z_d)$ to expression 5 gives the receiver-deghosted shot record

$$\mathbf{X}(z_d, z_s)\mathbf{G}(z_s, z_s)\vec{S}(z_s). \quad (6)$$

In practice, it is not straightforward to obtain the source-deghosted shot record from this expression because it must be multiplied from

the left by the matrix product: $\mathbf{X}(z_d, z_s)[\mathbf{G}(z_s, z_s)]^{-1}[\mathbf{X}(z_d, z_s)]^{-1}$. For the special case of a laterally invariant subsurface, the symmetric Toeplitz matrices $\mathbf{X}$ and $\mathbf{G}$ commute, that is, $\mathbf{X}(z_d, z_s)\mathbf{G}(z_s, z_s)\vec{S}(z_s) = \mathbf{G}(z_s, z_s)\mathbf{X}(z_d, z_s)\vec{S}(z_s)$, which simplifies shot record source deghosting. We will see this later in an example given in Figure 2.

In the case of ideal spatial source sampling, with unit sources, meaning that $\mathbf{S}(z_s) = \mathbf{I}$, the right side of equation 1 becomes

$$\mathbf{D}(z_d)\mathbf{G}(z_d, z_d)\mathbf{X}(z_d, z_s)\mathbf{G}(z_s, z_s). \qquad (7)$$

A receiver gather is represented by

$$\vec{D}^{\dagger}(z_d)\mathbf{G}(z_d, z_d)\mathbf{X}(z_d, z_s)\mathbf{G}(z_s, z_s), \qquad (8)$$

where the dagger symbol † indicates a row vector. Now, applying the inverse of $\mathbf{G}(z_s, z_s)$ to the above gives a source-deghosted receiver gather, which is given by

$$\vec{D}^{\dagger}(z_d)\mathbf{G}(z_d, z_d)\mathbf{X}(z_d, z_s). \qquad (9)$$

Again, it is not straightforward to obtain the receiver-deghosted receiver gather from expression 9. We transpose expression 9 to obtain

$$\mathbf{X}(z_d, z_s)^T\mathbf{G}(z_d, z_d)\vec{D}(z_d), \qquad (10)$$

using $\mathbf{G}(z_d, z_d) = \mathbf{G}(z_d, z_d)^T$ because of reciprocity, where superscript T indicates the transposed of a matrix. Now, the similarity with expression 6 is evident.

Above, we have formulated source deghosting carried out in the common-receiver domain (expressions 5 and 6) and receiver deghosting carried out in the common-shot domain (expressions 8 and 9). In the following section, numerical examples demonstrate that for a laterally invariant subsurface, source deghosting carried out in the common-shot domain is similar to source deghosting carried out in the common-receiver domain. However, for a complex subsurface, source deghosting carried out in the common-receiver domain is preferable to source deghosting carried out in the common-shot domain.

THE EFFECT OF A COMPLEX SUBSURFACE IN THE COMMON-SHOT DOMAIN

We first generated ghost-free 2D seismic data with a finite-difference scheme using the laterally invariant velocity model from Figure 1a. After that, we only added the source ghost using equation 3. For now, we did not model the receiver ghost because we first put all emphasis on the source ghost. Sources as well as receivers were located at a depth of 15 m with spatial sampling of 5 m. Figure 2a and 2b, respectively, shows a receiver gather and a shot record. As expected, they are identical. In Figure 2c and 2d, we show the corresponding representations in the wavenumber-frequency domain. The spectra have a clear first-order angle-dependent notch, which is
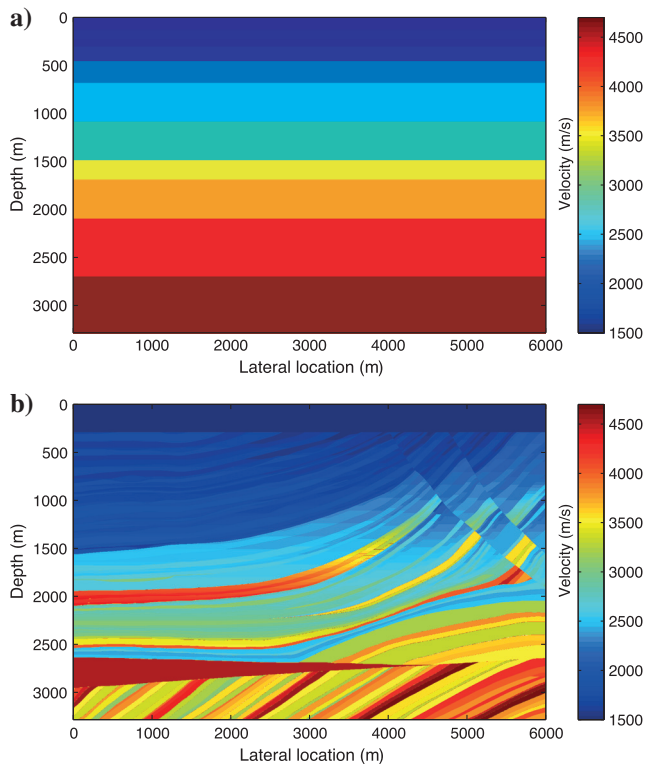

Figure 1. Velocity models used for acoustic finite-difference modeling. (a) Velocity model of a laterally invariant subsurface. (b) Velocity model of a complex subsurface (Marmousi model including a water layer on top).
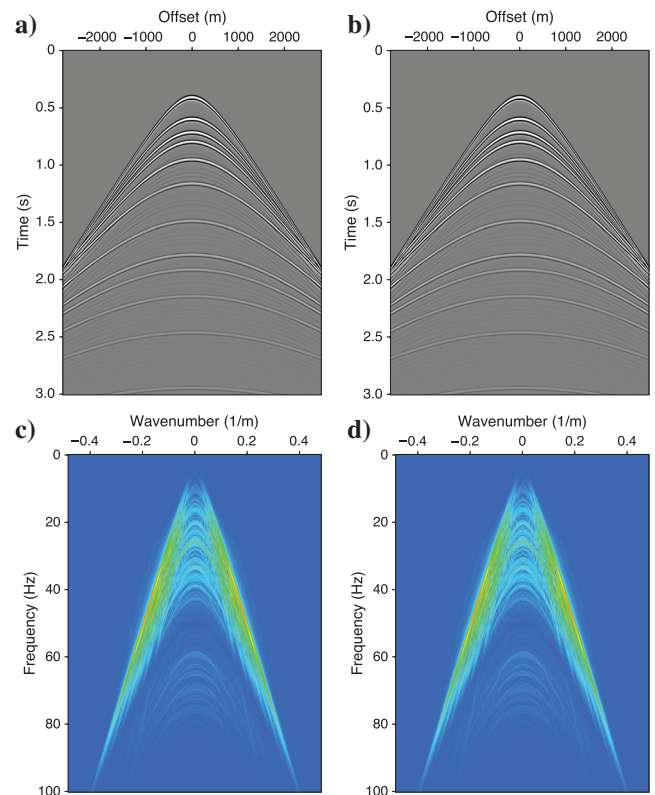

Figure 2. Data including the source-ghost wavefield in various domains for a laterally invariant model and a source depth of 15 m. (a) A receiver gather including the source ghost. (b) A shot record including the source ghost. (c) The wavenumber-frequency spectrum of the receiver gather including the source ghost. (d) The wavenumber-frequency spectrum of the shot record including the source ghost.

at 50 Hz for vertical wavefield propagation. This frequency can be easily computed from the water velocity c and the source depth z_s, being 1500 m/s and 15 m, respectively, via $f_{notch} = 0.5c/z_s$. The amplitude roll-off toward 0 Hz is the effect of the zeroth-order notch.

In the next example, we generated a similar data set, but now using the Marmousi subsurface model shown in Figure 1b rather than the laterally invariant subsurface model of Figure 1a. We show a receiver gather in Figure 3a and a shot record in Figure 3b. Unlike in the previous example, they are not identical. The difference in Figure 3c shows that the source-ghost wavefield, once observed in the common-shot domain, is affected by the complex subsurface. The first-order notch is clearly visible in the wavenumber frequency spectrum of a common-receiver gather (see Figure 3d). However, the first-order notch is blurred in the wavenumber frequency spectrum of a shot record (see Figure 3e).

Vrolijk and Blacquière (2020) give a detailed description of a deghosting algorithm based on sparse inversion as well as its adaptive variant. In Figure 4a, we show the result of applying the nonadaptive source deghosting variant to the receiver gather of Figure 3a. The difference with the original ghost-free data (see Figure 4b) is quantified by the signal-to-noise ratio (S/N) as follows:

$$S/N = 10 \log \left(\sum_x \sum_t \frac{|\rightarrow p_0|^2}{|\rightarrow p_0 - \langle \rightarrow p_0 \rangle|^2} \right), \qquad (11)$$

with $\vec{p}_0$ being the modeled ghost-free data and $\langle \rightarrow p_0 \rangle$ the deghosted result in the space-time domain. The overall S/N in this example is equal to 39.8 dB. A selected area with a time range of 2.2–2.6 s and an offset range of −2250 to −1250 m has an S/N of 39.8 dB, and another selected area with a time range of 1.52–1.92 s and offset range of 1000–2000 m has an S/N of 41.0 dB. The deghosting algorithm promotes sparsity in the space-time domain, which stabilizes the inversion. Therefore, no obvious deghosting artifacts are present in the data domain (see Figure 4a and 4b) and notches in the wavenumber-frequency domain are filled with the correct amplitudes (see Figure 4c and 4d).

We have demonstrated that the source-ghost wavefield, once observed in the common-shot domain, is affected by the complex subsurface. Consequently, this will have an effect on the quality of source deghosting in the common-shot domain, which we demonstrate in Figure 5. To obtain the result in Figure 5a, we applied the adaptive source-deghosting variant to the shot record of Figure 3b. This deghosting algorithm can adapt the depth of each source as a function of time. In this way, it can handle the source ghost observed in the common-shot domain, that is, after being affected by the complex earth, to some extent. The difference in Figure 5b shows that there are some weak ringing artifacts and amplitude losses. The corresponding wavenumber-frequency spectra of Figure 5a and 5b are shown in Figure 5c and 5d. The overall and selected S/Ns in Figure 5b are equal to, respectively, 9.0, 0.6, and 15.1 dB. These numbers are significantly lower than the S/Ns that we obtained in the common-receiver domain (Figure 4b). Hence, this example illustrates that it is essential that source deghosting is carried out in the common-receiver domain to obtain an optimal source-deghosted result.

THE EFFECT OF COARSELY SAMPLED DATA

We have demonstrated that source deghosting should be carried out in the common-receiver domain in the case of a complex subsurface to obtain optimum results. However, in practice, this domain is often coarsely sampled. This complicates source deghosting because this would cause aliasing artifacts. In Figure 6a, we show a coarsely sampled receiver gather from the Marmousi model with large spatial source sampling of 75 m. In practice, such a coarse source sampling often occurs in the crossline direction. The result is that the data are aliased, which leads to the well-known wrap-around effects in the wavenumber-frequency domain (see Figure 6d). Especially, the high frequencies are affected by the coarse sampling. Our sparse inversion deghosting method can handle coarsely sampled receiver gathers to some extent. The result is given in Figure 6b and 6e, respectively, the space-time and wavenumber-frequency domains. In Figure 6c and 6e, we show the difference with respect to the ghost-free data. The aliasing artifacts have a detrimental effect on the overall S/N, which is as low as −5.4 dB. The selected areas are affected as well (see Figure 6c). Thus, in case of coarsely sampled sources, we have to deal with the following dilemma. In the common-receiver domain, the quality of source deghosting is limited
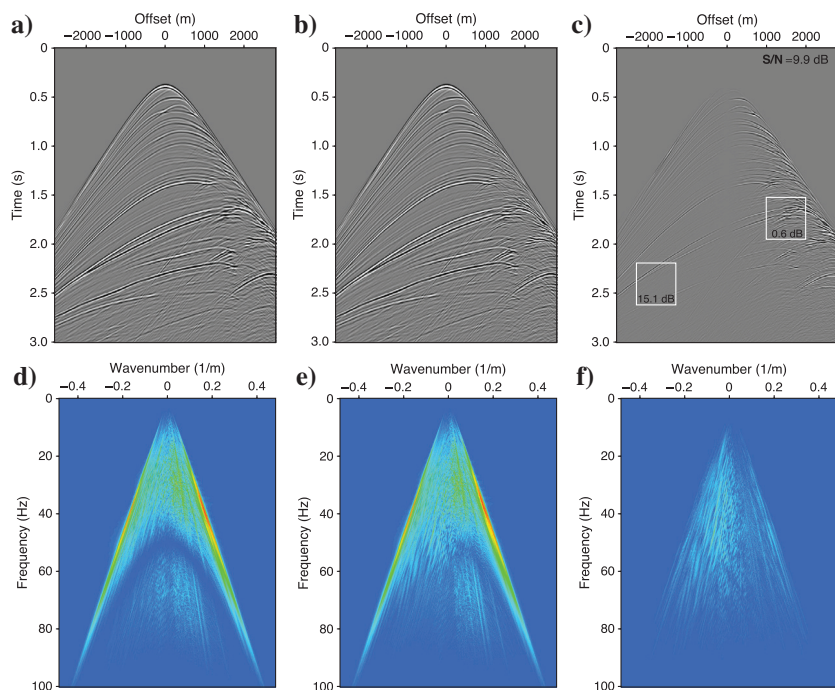
Figure 3. Data including the source-ghost wavefield in various domains for the Marmousi model and a source depth of 15 m. (a) A receiver gather including the source ghost. (b) A shot record including the source ghost. (c) The difference between (a and b). (d) The wavenumber-frequency spectrum of the receiver gather including the source ghost. (e) The wavenumber-frequency spectrum of the shot record including the source ghost. (f) The difference between (d and e).

by coarse source sampling, whereas in the common-shot domain the quality of source deghosting is limited by the complex subsurface. In the following section, we propose a machine-learning approach to handle this dilemma.

CNN SOURCE DEGHOSTING OF COARSELY SAMPLED COMMON-RECEIVER DATA

We have demonstrated that a coarse sampling in the common-receiver domain causes artifacts in the results of source deghosting. To overcome this issue, we propose to train a CNN with supervised learning to apply source deghosting to coarsely sampled receiver gathers. We start with the seismic data given by the following matrix product:

$$\mathbf{D}_\delta(z_d)\mathbf{G}(z_d, z_d)\mathbf{X}(z_d, z_s)\mathbf{G}(z_s, z_s)\mathbf{S}_\Delta(z_s), \quad (12)$$

where subscript Δ indicates a coarse sampling (here, for the sources), with spatial interval Δx, whereas subscript δ indicates a dense sampling (here for the receivers), with spatial interval δx. The relation between the two is given by $\Delta x = n\delta x$, where n is a positive integer.

The input training data consist of coarsely sampled shot records including the source-ghost wavefield as well as the receiver-ghost wavefield, whereas the output training data consist of receiver-deghosted coarsely sampled shot records. We apply the following processing steps to generate the training data. At first, we apply receiver deghosting to matrix product 12. After that, we redatum

the receivers to the level of the sources (see Figure 7a and 7b) using wavefield propagation on the pressure data, such that it becomes

$$\mathbf{D}_\delta(z_s)\mathbf{X}(z_s, z_s)\mathbf{G}(z_s, z_s)\mathbf{S}_\Delta(z_s). \quad (13)$$

In seismic acquisition, receivers are usually located below the source(s), and forward wavefield propagation must be carried out to obtain expression 13. In case receivers are located above the source, backward wavefield propagation must be carried out. Wavefield propagation is described by, for example, Wapenaar and Berkhout (1989) from a flat receiver level and by Sun et al. (2018) from an arbitrary receiver level. In this paper, we only use a forward propagation step in the field data example because in the other examples the sources and receivers are located on the same level. Forward propagation can be carried out accurately when receivers are sampled according to the Nyquist criterion. We then numerically add the receiver-ghost wavefield to obtain

$$\mathbf{D}_\delta(z_s)\mathbf{G}(z_s, z_s)\mathbf{X}(z_s, z_s)\mathbf{G}(z_s, z_s)\mathbf{S}_\Delta(z_s), \quad (14)$$

where the receiver-ghost wavefield is now related to the level of the sources. This step ensures that the shot records of matrix product 14, being our training data, are similar to the receiver gathers of matrix product 14, except that their spatial sampling is different. In the next step, we subsample the receivers of matrix products 13 and 14 such that the spatial receiver sampling becomes identical to the coarse source sampling (see Figure 7c). Given that n is the upsampling
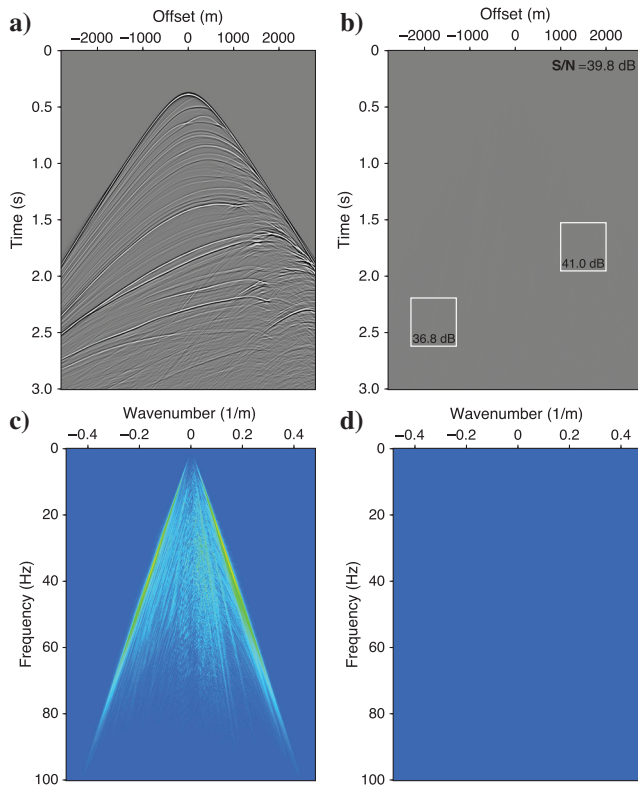

Figure 4. The source-deghosting result based on sparse inversion of the data shown in Figure 3a. (a) Common-receiver gather after source deghosting. (b) The difference between (a) and the modeled ghost-free receiver gather. (c) The wavenumber-frequency spectrum of (a). (d) The wavenumber-frequency spectrum of (b).
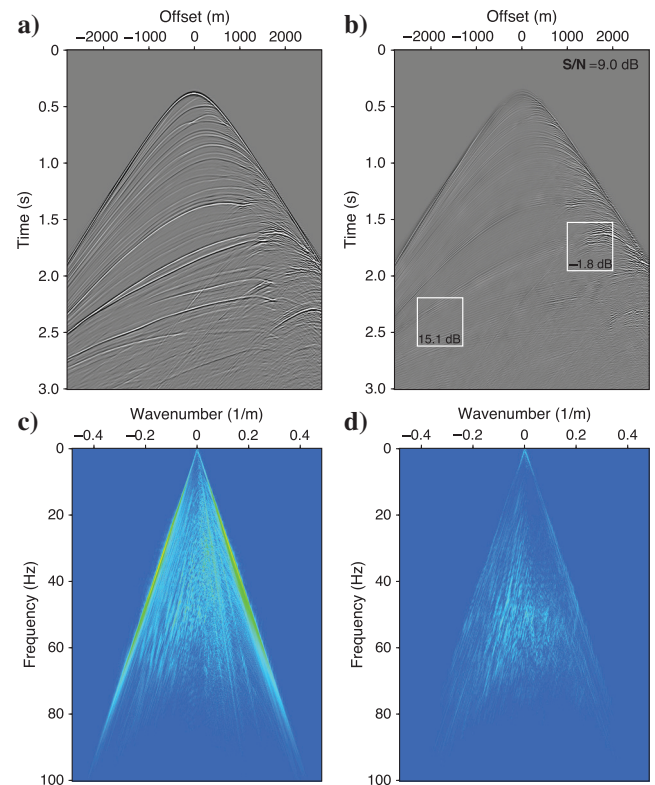

Figure 5. The adaptive source-deghosting result of Figure 3b. (a) Shot record after source deghosting. (b) The difference between (a) and the modeled ghost-free shot record. (c) The wavenumber-frequency spectrum of (a). (d) The wavenumber-frequency spectrum of (b).
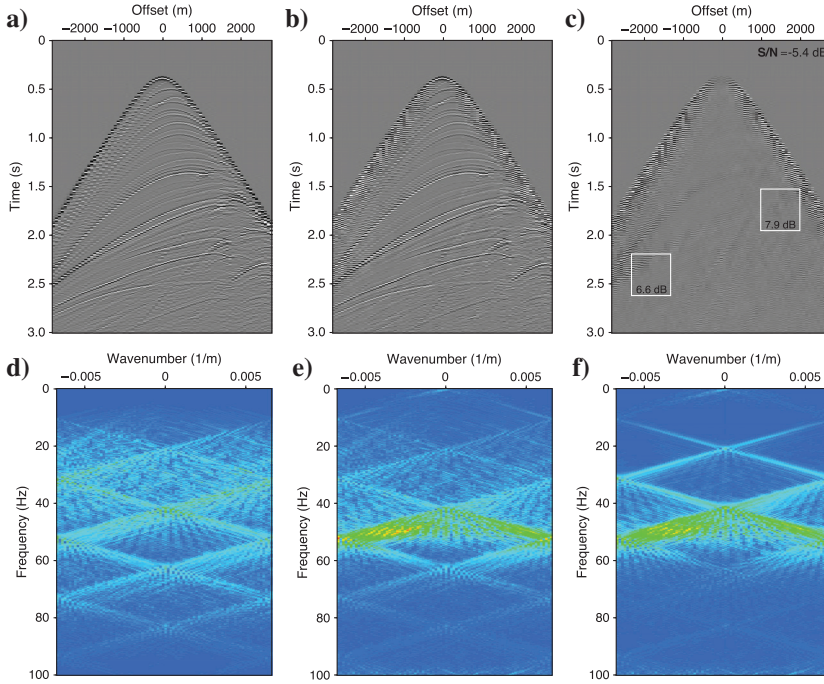
Figure 6. (a) Modeled, coarsely sampled, ghost-free common-receiver gather. (b) Common-receiver gather after deghosting. (c) The difference between (a and b). (d) The wavenumber-frequency spectrum of (a). (e) The wavenumber-frequency spectrum of (b). (f) The wavenumber-frequency spectrum of (c).
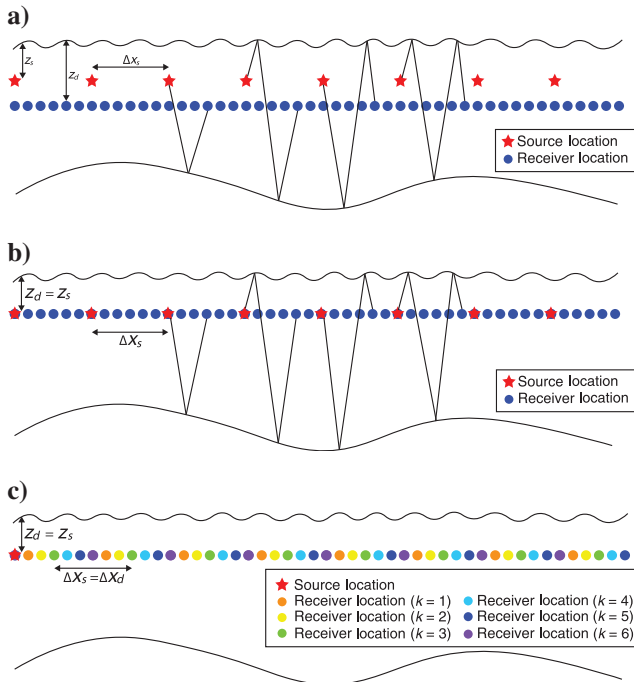

Figure 7. The preprocessing steps to obtain the training data. The four raypaths in (a and b) are, respectively, the direct event, the source ghost, the receiver ghost, and the source-receiver ghost. (a) The coarsely sampled sources at source level z_s and densely sampled receivers at receiver level z_d. (b) The original receiver ghost is replaced with a receiver ghost that corresponds to receivers at the depth level of the sources ($z_d = z_s$). (c) A densely sampled shot record is subsampled for $n = 6$.

rate between the source and the receiver sampling, the index k of the first detector can have values ranging from 1 to n. This means that n different subsampled data sets can be made of each shot record. Only if the source and receiver locations coincide is the data set reciprocal (see $k = 1$ in Figure 7c). The n subsampled data sets, being the input training data, are obtained from matrix product 14 and can be formulated as

$$[\mathcal{X}^{\text{train}}]_k = [\mathbf{D}_\Delta(z_s)]_k \mathbf{G}(z_s, z_s) \mathbf{X}(z_s, z_s)$$
$$\times \mathbf{G}(z_s, z_s) \mathbf{S}_\Delta(z_s), \quad \text{for } k = 1, 2, \ldots, n. \tag{15}$$

To obtain the output training data, we subsample the receivers of matrix product 13 such that

$$[\mathcal{Y}^{\text{train}}]_k = [\mathbf{D}_\Delta(z_s)]_k \mathbf{X}(z_s, z_s)$$
$$\times \mathbf{G}(z_s, z_s) \mathbf{S}_\Delta(z_s), \quad \text{for } k = 1, 2, \ldots, n. \tag{16}$$

The CNN handles each shot record combination from equation 15 with the receiver ghost and 16 without the receiver ghost as an individual training pair. Once the network has been trained, we apply the network to remove the source-ghost wavefield from the transpose of matrix product 15, which is given by

$$[\mathcal{X}]_k = \mathbf{S}_\Delta(z_s)^T \mathbf{G}(z_s, z_s) \mathbf{X}(z_s, z_s) \mathbf{G}(z_s, z_s) [\mathbf{D}_\Delta(z_s)]_k^T,$$
$$\text{for} \quad k = 1, 2, \ldots, n. \tag{17}$$

Notice the similarity with equation 15. Therefore, we can now use the CNN to carry out the source deghosting, which results in

$$[\mathcal{Y}]_k = \mathbf{S}_\Delta(z_s)^T \mathbf{X}(z_s, z_s) \mathbf{G}(z_s, z_s) [\mathbf{D}_\Delta(z_s)]_k^T,$$
$$\text{for } k = 1, 2, \ldots, n. \tag{18}$$

Undoing the transposition and using $\mathbf{D}_\delta = \sum_{k=1}^{n} \mathbf{D}_\Delta$, we obtain

$$\mathbf{D}_\delta(z_s) \mathbf{G}(z_s, z_s) \mathbf{X}(z_s, z_s) \mathbf{S}_\Delta(z_s), \tag{19}$$

which, after conventional receiver deghosting carried out on the well-sampled shot records, becomes

$$\mathbf{D}_\delta(z_s) \mathbf{X}(z_s, z_s) \mathbf{S}_\Delta(z_s). \tag{20}$$

If desired, this can be redatumed to $\mathbf{D}_\delta(z_d) \mathbf{X}(z_d, z_s) \mathbf{S}_\Delta(z_s)$, which represents the fully deghosted version of equation 1. In this section we have described an approach that allows us to train a network from the same data distribution that the network will ultimately be applied to, which will contribute to the reliability of the network.

CNN ARCHITECTURE

The CNN architecture used in this paper is based on the work of Ronneberger et al. (2015) and Quan et al. (2016) on convolutional encoder-decoder networks. These networks have been applied

successfully in the medical field with a limited amount of training data and in terms of the amount of data that resembles our case. The network consists of four encoding layers and four decoding layers connected by a bridge (see Figure 8). Each encoding layer consists of a convolutional layer, a batch normalization layer, an activation layer, and a max pooling layer. The max pooling layer downsamples the data with a factor of two in the time and space dimensions. Each decoding layer consists of a transposed convolutional layer, a batch normalization layer, and an activation layer. The transposed convolutional layer upsamples the data and makes sure that the number of filters is equal to its connected encoding layer. The encoding layers are connected with a summation to a corresponding decoding layer, which makes the network fully residual. The components of the bridge are similar to those of the encoding layer, but without a max pooling layer. The number of filters gradually increases toward the bridge block and then gradually decreases toward the predicted output. The activation layer consists of a rectified linear unit (ReLU) function. We used the stochastic gradient descent to minimize the L2-misfit between the training input and the training output. In addition, we modified the size of the kernel to handle the seismic data properly.

CNN SOURCE DEGHOSTING: NUMERICAL EXAMPLE

To obtain the training data, we first modeled ghost-free seismic data for the Marmousi velocity model shown in Figure 1b using a fixed spread configuration. In total, we modeled 1200 sources and 1200 receivers on a grid of $\delta x = 5$ m, which allowed us to add both ghost wavefields as explained earlier. The ghost wavefields correspond to sources and receivers located at $z_s = z_d = 15$ m under the sea surface. Then, we applied source subsampling with a factor $n = 15$, from $\delta x = 5$ m to $\Delta x = 75$ m to obtain 80 modeled shot records. Because we put the sources and receivers on the same level, redatuming is unnecessary and we created a situation as illustrated in Figure 7b. After that, we subsample the receivers of these 80 modeled shot records with a factor $n = 15$ for each index k to obtain the input training data (see Figure 7c). To obtain the output training data, we applied receiver deghosting before the receiver subsampling stage. In total, we used 1200 training pairs, which is equal to 80 shot records times n. We created an additional 300 pairs from the dense data excluding the 80 shot records used for training to validate the network and to determine the number of filters, number of layers, and the learning rate. We show the performance on the training and validation data in Table 1. These results indicate that the performance of the network is quite robust with respect to changes in the learning rate and the size of the network. Only the results obtained with a smaller amount of filters significantly reduced the performance of the network. The results that we show in the

data and frequency domain are obtained using a CNN with four encoding layers, four decoding layers, and a learning rate of 0.01. The number of filters increases from 64 to 1024 at the bridge block, after which the filter size recursively decreases to 64.

In Figure 9a, we show a subsampled receiver-deghosted shot record with a lateral source position of 2925 m. After training (100 epochs), the differences between the CNN receiver-deghosted shot record and its corresponding training output have an overall S/N of 29.2 dB and S/Ns of, respectively, 29.8 and 24.8 dB for the selected areas (see Figure 9c).

In Figure 9b, we show a subsampled validation record with a lateral source position of 4325 m. The differences in the selected areas with the modeled source-ghost-free receiver gathers in Figure 9d have S/Ns of 18.4 and 22.2 dB and an overall S/N of
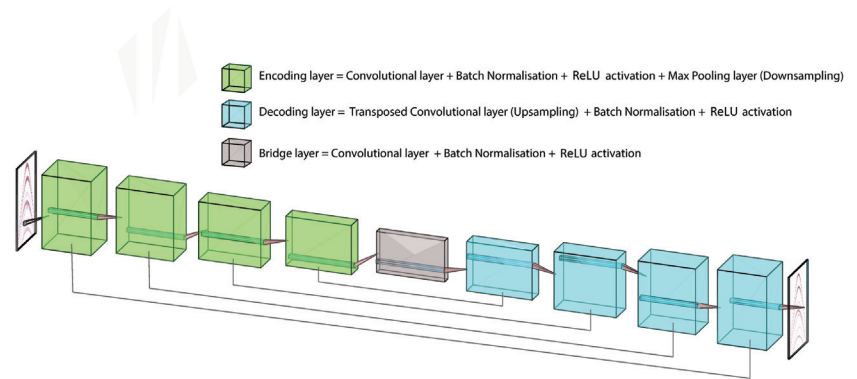

Figure 8. The architecture of the CNN, showing the encoder-decoder structure and the residual connections between each encoding and decoding block.

Table 1. The sensibility of the overall CNN performance of the training data, validation data, and application data with respect to the number of layers, the learning rate, and the filter numbers.

Network performance (dB)

| Network parameters	Training data (1200 pairs)	Validation data (300 pairs)	Application data (1200 pairs)
Encoding layers = 4 Decoding layers = 4	27.4	23.3	22.6
Learning rate = 0.01			
Filter numbers = 64, 128, 256, 512, and 1024			
Encoding layers = 4 Decoding layers = 4	27.0	23.2	22.5
Learning rate = 0.001			
Filter numbers = 64, 128, 256, 512, and 1024			
Encoding layers = 4 Decoding layers = 4	21.6	20.9	20.5
Learning rate = 0.01			
Filter numbers = 16, 32, 64, 128, and 256			
Encoding layers = 3 Decoding layers = 3	26.7	23.2	22.5
Learning rate = 0.01			
Filter numbers = 64, 128, 256, 512, and 1024			
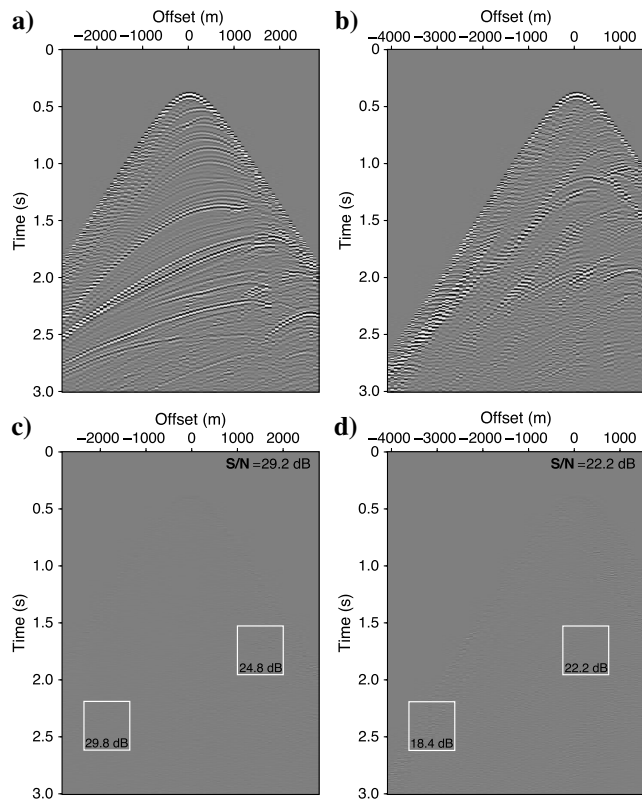
Figure 9. The results of the CNN for one input training shot record and one validation shot record. (a) Training shot record (lateral source location: 2925 m) after CNN receiver deghosting. (b) Validation shot record with source (lateral source location: 4325 m) after CNN receiver deghosting. (c) The difference between (a) and the corresponding output training shot record. (d) The difference between (b) and the corresponding output validation shot record.
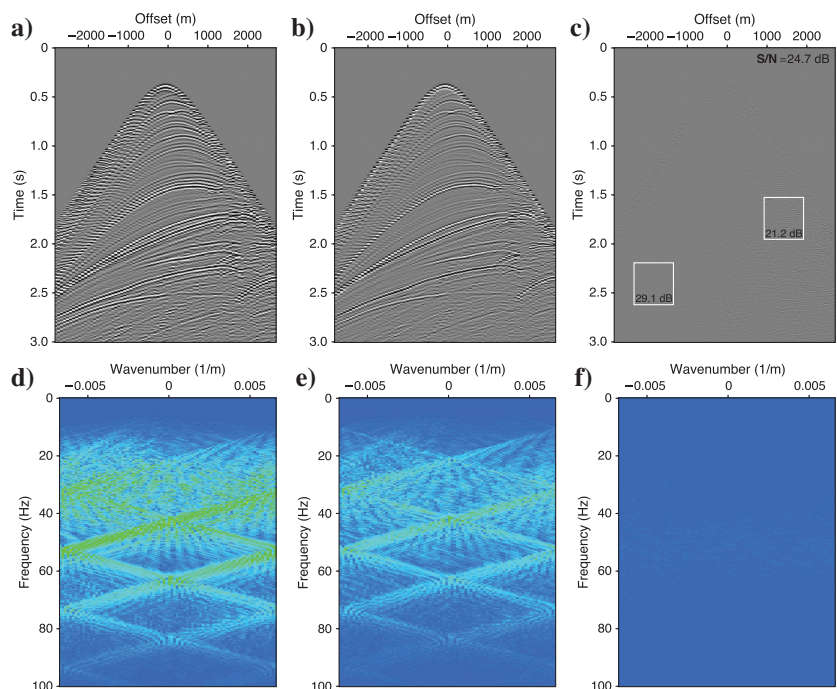
22.2 dB. We applied the CNN to remove the source-ghost wavefield from the original 1200 coarsely sampled receiver gathers as well. We show examples in Figures 10 and 11 for receiver gathers with lateral receiver locations of 2890 and 4750 m, respectively. Note that the receiver ghost is still present. The differences in Figures 10c and 11c have S/Ns between 16.0 and 29.1 dB. The wavenumber-frequency spectra show that there is only a small amount of residual energy around the notch frequency of 50 Hz related to vertical propagation (see Figures 10f and 11f). The CNN result gives a significant uplift compared to the source-deghosted result of Figure 6b. Note that the overall performance on the application data is comparable to the overall performance on the validation data (see Table 1).

In Figure 12a, we show a shot record corresponding to Figures 10b and 11b. Next, we applied receiver deghosting based on sparse inversion to the well-sampled source-deghosted shot records, leading to fully deghosted records. An example of a shot record before and after receiver deghosting can be found in Figure 12a and 12b. The corresponding wavenumber-frequency spectra are shown in Figure 12d and 12e. The difference with the modeled ghost-free shot gather is shown in Figure 12c and 12f. The selected areas in Figure 12c have S/Ns of 20.3 and 26.6 dB and an overall S/N of 20.6 dB. Again, the results of the CNN have a higher S/N than the conventional deghosting result shown in Figure 7a. This is due to the latter method being carried out in the "wrong" domain, which limits its quality, while the CNN does not suffer from this issue.

CNN source deghosting: Field data example

We applied the machine-learning approach for applying source deghosting to coarsely sampled receiver gathers taken from a field data set, acquired offshore Australia. For this example, we took a subset of 110 shot records with a spatial source sampling of $\Delta x = 75$ m and a spatial receiver sampling of $\delta x = 6.25$ m, meaning that $n = 12$ in this example. The source depth was 5 m, and the depth of

Figure 10. The CNN result for a coarsely sampled receiver gather with a lateral receiver location at 2890 m. (a) Receiver gather including the source as well as the receiver ghost. (b) Receiver gather after CNN source deghosting. (c) The difference between (b) and the modeled source-ghost-free receiver gather. (d-f) The wavenumber-frequency spectra of (a-c).

the slanted cable ranged from 8 to 60 m. A single shot record is shown in Figure 13a, and its wavenumber-frequency spectrum is shown in Figure 14a. Due to the slant of the cable, which leads to notch diversity, there is no clear receiver-ghost notch in the wavenumber-frequency spectrum. Figures 13b and 14b show the result after receiver deghosting. The arrows in Figure 13a and 13b indicate that the slanted ghost effect is removed accurately. In addition, the receivers have been redatumed to the source level of 5 m. We then numerically added the corresponding receiver-ghost wavefield (see

Figure 13c). As expected, now a clear first-order receiver-ghost notch becomes visible in the spectrum at approximately 150 Hz for vertical propagation (see Figure 14c). To create the training data for the CNN, we subsampled the shot records with and without the redatumed receiver-ghost wavefield by the factor of $n = 12$. The number of layers, the number of filters, and the learning rate remain the same as in the numerical example discussed previously. Only the size of the kernels was adjusted to the size of the subsampled shot records from the field data. Once the network was trained (after
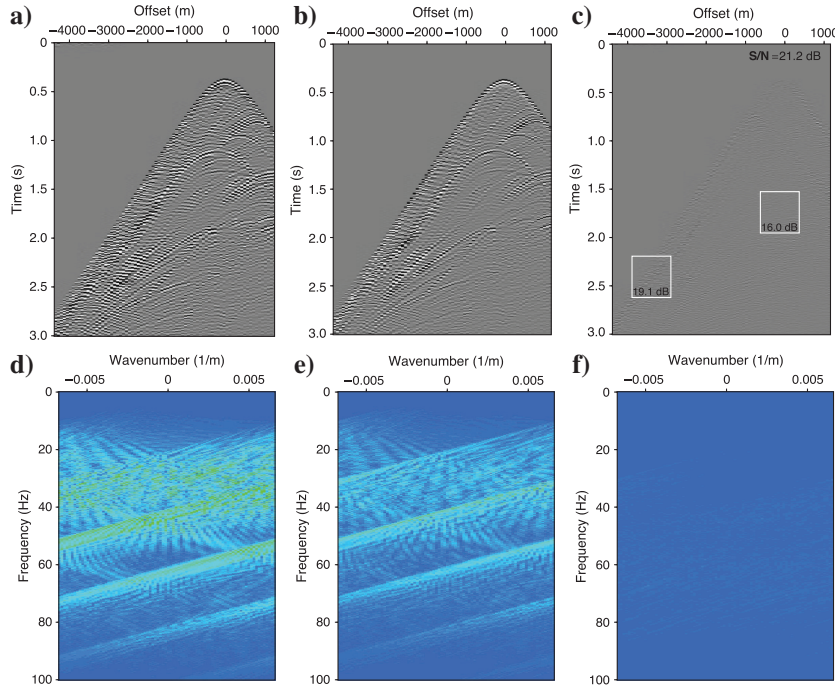

Figure 11. The CNN result for a coarsely sampled receiver gather with a lateral receiver location at 4750 m. (a) Receiver gather including the source as well as the receiver ghost. (b) Receiver gather after CNN source deghosting. (c) The difference between (b) and the modeled source-ghost-free receiver gather. (d-f) The wavenumber-frequency spectra of (a-c).
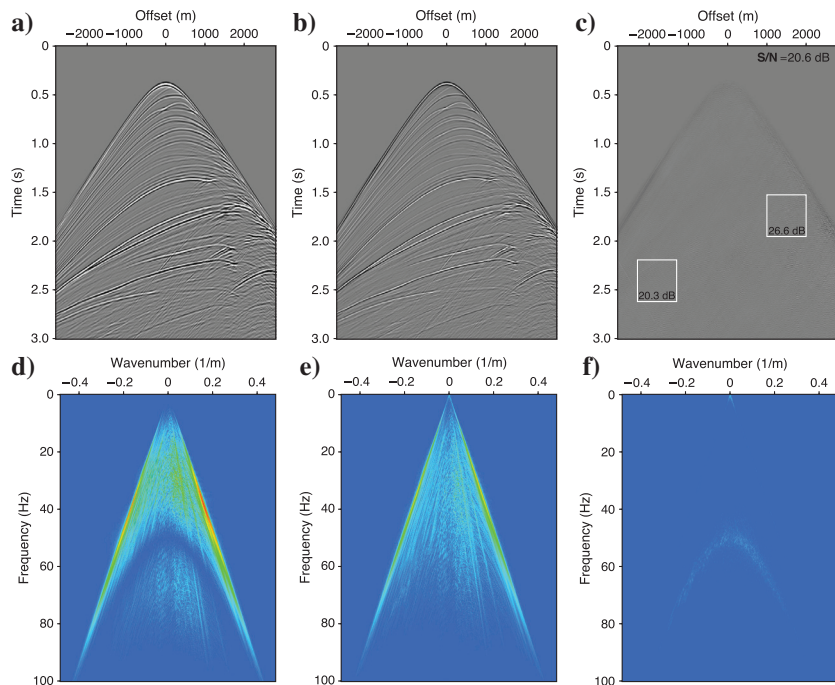

Figure 12. Receiver deghosting after source deghosting. (a) Input: shot record after CNN source deghosting carried out in the common-receiver domain. (b) Output: shot record of (a) after receiver deghosting using sparse inversion carried out in the common-shot domain. (c) The difference between (b) and the modeled ghost-free shot record. (d-f) The wavenumber-frequency spectra of (a-c).

200 epochs) with the subsampled shot records, we applied the CNN to remove the source ghost from the coarsely sampled receiver gathers.

We then carried out receiver deghosting using sparse inversion in the densely sampled common-shot domain. A shot record from the now fully deghosted result is shown in Figure 13d. The reflections have the high-resolution appearance that characterizes ghost-free wide-band data, without any obvious deghosting artifacts. The corresponding wavenumber-frequency domain representation is shown in Figure 14d. As expected, we see that the amplitudes around the zeroth- and first-order source-ghost notches, at 0 and 150 Hz, respectively, have been boosted, whereas in between these notches the amplitudes have been reduced. Thus, the shot-record and its wavenumber-frequency spectrum indicate that the source ghost and the receiver ghost have been removed successfully.

A conventional technique to obtain the source-deghosted result is to apply trace-by-trace sparse deghosting with a 1D ghost model. We compare results obtained with trace-by-trace sparse source deghosting with results obtained with CNN source deghosting for a shallow near-offset section in the common-shot domain with a minimum offset of 175 m (Figure 15a and 15b). The trace-by-trace sparse source deghosting-result has some deghosting artifacts, which are most visible near the water-bottom reflection. These artifacts might be related to the relatively weak angle-dependency of the ghost. They are not present in the CNN source-deghosting result. As an additional quality control, we compare the correspond-

ing stacked frequency spectra of Figure 15a and 15b in Figure 16. We also show the frequency spectrum before source deghosting. Figure 16 shows that the observed artifacts after trace-by-trace source deghosting are the result of overamplified amplitudes in the notch area, which confirms that these artifacts are the result of neglecting the angle dependency of the ghost.

DISCUSSION

This paper demonstrated the capabilities of a machine-learning approach for removing the source-ghost wavefield from coarsely sampled data. It is a first step toward a fully 3D source wavefield deghosting method that is suitable for coarsely sampled data. Other

Figure 14. (a) The wavenumber-frequency spectrum of Figure 13a. (b) The wavenumber-frequency spectrum of Figure 13b. (c) The wavenumber-frequency spectrum of Figure 13c. (d) The wavenumber-frequency spectrum of Figure 13d.
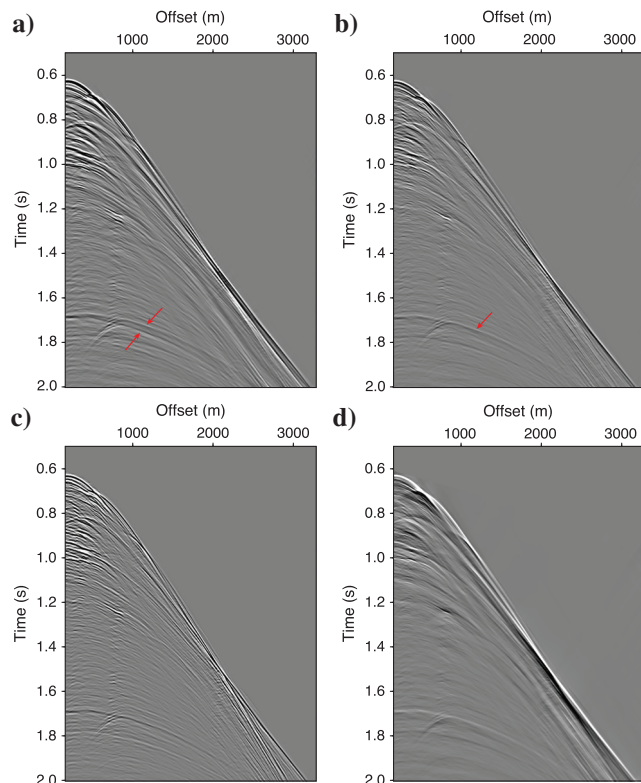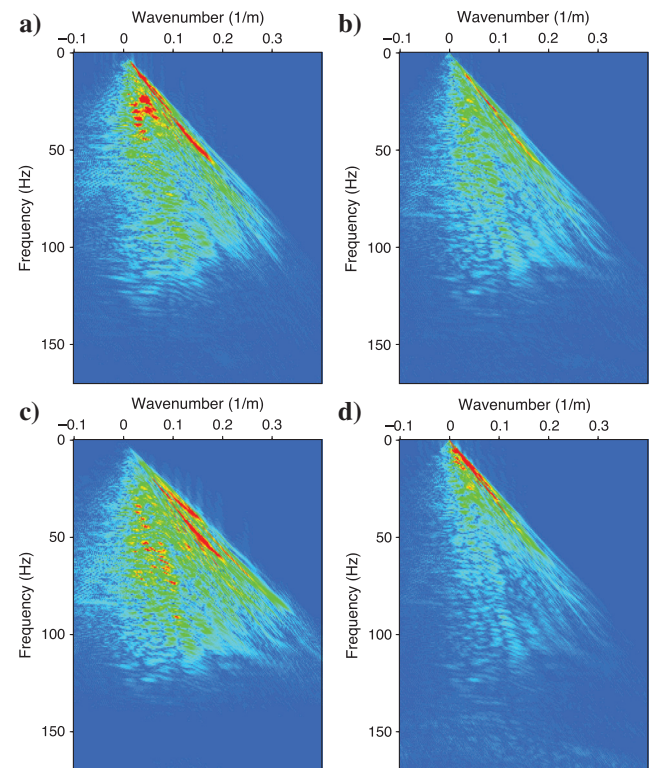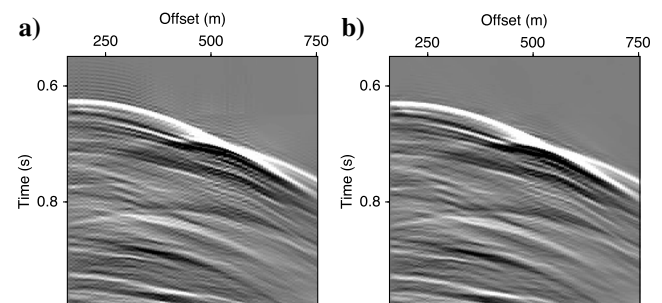

Figure 13. (a) Shot record including the source-ghost effect as well as the slanted-cable receiver ghost effect. (b) Redatumed shot record including the source-ghost effect. (c) Redatumed shot record including the source-ghost effect as well as the modeled receiver ghost effect. (d) The shot record after CNN source deghosting and conventional receiver deghosting.

Figure 15. (a) A near-offset section after sparse receiver deghosting and trace-by-trace sparse source deghosting. (b) A near-offset section sparse receiver deghosting and CNN source deghosting.
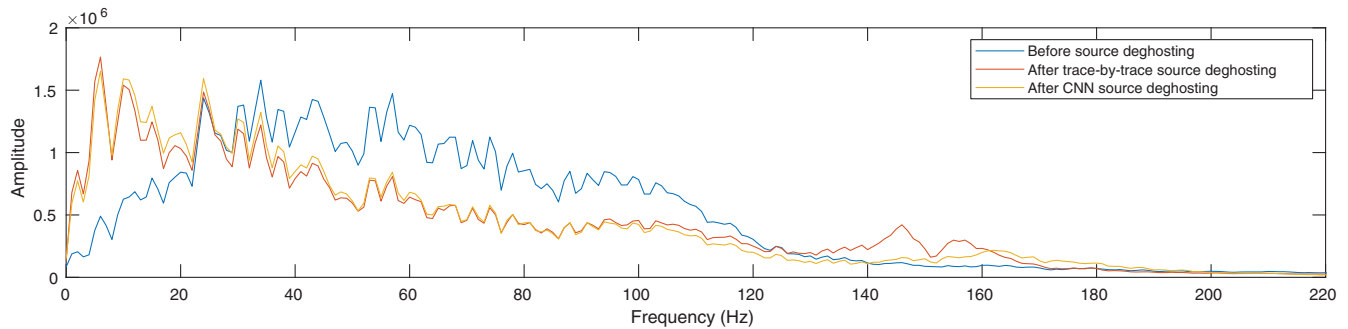
Figure 16. The stacked frequency spectra corresponding to Figure 15a and 15b and before receiver deghosting.

seismic processing methods such as source redatuming, which are limited by coarsely sampled data, might benefit from a comparative strategy. One of the challenges in 3D would be the different azimuth distribution between the redatumed and subsampled shot gathers and the aliased receiver gathers. In principle, the method can handle irregular geometries by adjusting the subsampling or, if necessary, interpolating the training data to the required irregular sampling geometry. Another challenge is to account for variations between the source and receiver ghost wavefield due to rough sea surface effects. A rough sea surface causes asymmetry between the source ghost and the receiver ghost throughout a survey. The source ghost is almost instantaneous; therefore, it is accurately described by an effective static sea surface model. However, the receiver ghost could only be handled by a dynamic sea surface model. In such a case, the receiver ghost must first be removed using a method that can handle a dynamic rough sea surface (King and Poole, 2015; Grion et al., 2016; Vrolijk and Blacquière, 2020). Subsequently, an effective static sea surface model could be included during the modeling of the receiver-ghost wavefield on the source depth. It is also known that, for example, ghost cavitation causes asymmetry between the source side and the receiver side. The field-data results indicated that the CNN might be able to deal with the nonlinear source effects because no obvious deghosting artifacts effects were present. Including the exact source effects, azimuthal differences, and rough sea surface effects in the training data could be challenging, and further research is required. In addition, comparing our proposed method with existing deep learning interpolation schemes (Garg et al., 2019; Siahkoohi et al., 2019a; Wang et al., 2020) followed by, for example, a sparse source-deghosting method could also provide more insight into its capabilities.

It is expected that the method can be easily adapted to be suitable for application to coarsely sampled common-shot gathers acquired with ocean-bottom nodes. After source deghosting and redatuming of the sources to the ocean bottom, the training of the CNN can be carried out on subsampled common-receiver gathers with and without a modeled source-ghost wavefield. Then, the CNN could be applied to coarsely sampled common-shot gathers to remove the receiver-ghost wavefield.

CONCLUSION

We have successfully applied a CNN to remove the source-ghost wavefield from coarsely sampled receiver gathers. The key is that we used the symmetry that exists between source deghosting in the common-receiver domain and receiver deghosting in the common-

shot domain. Because receiver deghosting in the well-sampled common-shot domain is relatively easy, we proposed a strategy to train the CNN with subsampled shot records before and after receiver deghosting. Because of the symmetry, this case mimics the situation of coarsely sampled receiver gathers before and after source deghosting. Tests on numerical as well as field data show that our approach can accurately remove the source-ghost wavefield from coarsely sampled receiver gathers. These results are better than those obtained from adaptive source deghosting in the well-sampled common-shot domain.

ACKNOWLEDGMENTS

DATA AND MATERIALS AVAILABILITY

Data associated with this research are confidential and cannot be released.

REFERENCES

Araya-Polo, M., J. Jennings, A. Adler, and T. Dahlke, 2018, Deep-learning tomography: The Leading Edge, **37**, 58–66, doi: 10.1190/tle37010058.1.
Berkhout, A. J., 1985, Seismic migration, Part A: Theoretical aspects, 3rd ed.: Elsevier.
Blacquière, G., and H. Ö. Sertlek, 2019, Modeling and assessing the effects of the sea surface, from being flat to being rough and dynamic: Geophysics, **84**, no. 2, T13–T27, doi: 10.1190/geo2018-0294.1.
Caporal, M., G. Blacquière, and M. Davydenko, 2018, Broadband imaging via direct inversion of blended dispersed source array data: Geophysical Prospecting, **66**, 942–953, doi: 10.1111/1365-2478.12584.
Das, V., A. Pollack, U. Wollner, and T. Mukerji, 2019, Convolutional neural network for seismic impedance inversion: Geophysics, **84**, no. 6, R869–R880, doi: 10.1190/geo2018-0838.1.
Day, A., T. Klüver, W. Söllner, H. Tabti, and D. Carlson, 2013, Wavefield-separation methods for dual-sensor towed-streamer data: Geophysics, **78**, no. 2, WA55–WA70, doi: 10.1190/geo2012-0302.1.
Garg, A., A. Vos, N. Bortych, D. Gupta, and D. Verschuur, 2019, Spatial aliasing removal using deep learning super-resolution: First Break, **37**, 87–92.
Glinsky, M. E., G. A. Clark, P. K. Z. Cheng, K. R. S. Devi, J. H. Robinson, and G. E. Ford, 2001, Automatic event picking in prestack migrated gathers using a probabilistic neural network: Geophysics, **66**, 1488–1496, doi: 10.1190/1.1487094.
Grion, S., R. Telling, and S. Holland, 2016, Rough sea estimation for phase-shift deghosting: 86th Annual International Meeting, SEG, Expanded Abstracts, 5129–5133, doi: 10.1190/segam2016-13688475.1.
Hampson, G., 2017, Notional ghosts: 87th Annual International Meeting, SEG, Expanded Abstracts, 111–115, doi: 10.1190/segam2017-17634121.1.

Hopperstad, J.-F., R. Laws, and E. Kragh, 2008, Where is the center of a multi-depth marine source array? 78th Annual International Meeting, SEG, Expanded Abstracts, 40–44, doi: 10.1190/1.3054834.

Huang, L., X. Dong, and T. E. Clee, 2017, A scalable deep learning platform for identifying geologic features from seismic attributes: The Leading Edge, **36**, 249–256, doi: 10.1190/tle36030249.1.

Khodabandeloo, B., and M. Landrø, 2018, Acoustically induced cavity cloud generated by air-gun arrays — Comparing video recordings and acoustic data to modeling: Journal of Acoustical Society of America, **143**, 3383, doi: 10.1121/1.5040490.

King, S., and G. Poole, 2015, Hydrophone-only receiver deghosting using a variable sea surface datum: 85th Annual International Meeting, SEG, Expanded Abstracts, 4610–4614, doi: 10.1190/segam2015-5891123.1.

Kryvohuz, M., and X. Campman, 2017, Source-side up-down wavefield separation using dual NFHs: 79th Annual International Conference and Exhibition, EAGE, Extended Abstracts, 111–115, doi: 10.3997/2214-4609.201700843.

Landrø, M., L. Amundsen, and D. Barker, 2011, High-frequency signals from air-gun arrays: Geophysics, **76**, no. 4, Q19–Q27, doi: 10.1190/1.3590215.

Lewis, W., and D. Vigh, 2017, Deep learning prior models from seismic images for full-waveform inversion: 87th Annual International Meeting, SEG, Expanded Abstracts, 1512–1517, doi: 10.1190/segam2017-17627643.1.

Mikhailiuk, A., and A. Faul, 2018, Deep learning applied to seismic data interpolation: 80th Annual International Conference and Exhibition, EAGE, Extended Abstracts, 1–5, doi: 10.3997/2214-4609.201800918.

Nath, S. K., S. Chakraborty, S. K. Singh, and N. Ganguly, 1999, Velocity inversion in cross-hole seismic tomography by counter-propagation neural network, genetic algorithm and evolutionary programming techniques: Geophysical Journal International, **138**, 108–124, doi: 10.1046/j.1365-246x.1999.00835.x.

Parkes, G., and S. Hegna, 2011, A marine seismic acquisition system that provides a full 'ghost-free' solution: 81st Annual International Meeting, SEG, Expanded Abstracts, 37–41, doi: 10.1190/1.3627998.

Parkes, G. E., and L. Hatton, 1986, The marine seismic source: Seismology and exploration geophysics: Reidel.

Pham, N., S. Fomel, and D. Dunlap, 2019, Automatic channel detection using deep learning: Interpretation, **7**, no. 3, SE43–SE50, doi: 10.1190/INT-2018-0202.1.

Quan, T. M., D. G. C. Hildebrand, and W.-K. Jeong, 2016, Fusionnet: A deep fully residual convolutional neural network for image segmentation in connectomics: arXiv preprints, arXiv:1612.05360.

Ronneberger, O., P. Fischer, and T. Brox, 2015, U-Net: Convolutional networks for biomedical image segmentation: Medical Image Computing and Computer-Assisted Intervention, 234–241.

Ross, C. P., and D. M. Cole, 2017, A comparison of popular neural network facies-classification schemes: The Leading Edge, **36**, 340–349, doi: 10.1190/tle36040340.1.

Röth, G., and A. Tarantola, 1994, Neural networks and inversion of seismic data: Journal of Geophysical Research: Solid Earth, **99**, 6753–6768, doi: 10.1029/93JB01563.

Shi, Y., X. Wu, and S. Fomel, 2018, Automatic salt-body classification using deep-convolutional neural network: 88th Annual International Meeting, SEG, Expanded Abstracts, 1971–1975, doi: 10.1190/segam2018-2997304.1.

Siahkoohi, A., R. Kumar, and F. J. Herrmann, 2019a, Deep-learning based ocean bottom seismic wavefield recovery: 89th Annual International Meeting, SEG, Expanded Abstracts, 2232–2237, doi: 10.1190/segam2019-3216632.1.

Siahkoohi, A., D. J. Verschuur, and F. J. Herrmann, 2019b, Surface-related multiple elimination with deep learning: 89th Annual International Meeting, SEG, Expanded Abstracts, 4629–4634, doi: 10.1190/segam2019-3216723.1.

Sun, H., and L. Demanet, 2018, Low-frequency extrapolation with deep learning: 88th Annual International Meeting, SEG, Expanded Abstracts, 2011–2015, doi: 10.1190/segam2018-2997928.1.

Sun, Y., and D. Verschuur, 2017, 3D receiver deghosting for seismic-streamer data using L1 inversion in an extended Radon space: 87th Annual International Meeting, SEG, Expanded Abstracts, 4940–4944, doi: 10.1190/segam2017-17335240.1.

Sun, Y., D. J. Verschuur, and R. G. van Borselen, 2018, Acoustic propagation operators for pressure waves on an arbitrarily curved surface in a homogeneous medium: Journal of Applied Geophysics, **150**, 314–324, doi: 10.1016/j.jappgeo.2017.11.007.

Tang, Z., and X. Campman, 2017, Joint up/down decomposition and reconstruction using three-component streamers with or without ghost model: The sampling theory: Geophysical Prospecting, **65**, 956–980, doi: 10.1111/1365-2478.12438.

Telling, R., and S. Grion, 2019, A perturbed ghost model for estimating air-gun array signatures: The Leading Edge, **38**, 692–696, doi: 10.1190/tle38090692.1.

Tenghamn, R., S. Vaage, and C. Borresen, 2007, A dual-sensor towed marine streamer: Its viable implementation and initial results: 77th Annual International Meeting, SEG, Expanded Abstracts, 989–993, doi: 10.1190/1.2792571.

Vrolijk, J. W., and G. Blacquière, 2020, Adaptive estimation of the upgoing wavefield from a variable-depth recording in the case of a dynamic sea surface: Geophysics, **85**, no. 1, V45–V56, doi: 10.1190/geo2019-0035.1.

Walker, C. D. T., D. J. Monk, and D. B. Hays, 2014, Blended source — The future of ocean bottom seismic acquisition: 76th Annual International Conference and Exhibition, EAGE, Extended Abstracts, 1–5, doi: 10.3997/2214-4609.20141470.

Wang, B., N. Zhang, W. Lu, J. Geng, and X. Huang, 2020, Intelligent missing shots reconstruction using the spatial reciprocity of Green's function based on deep learning: IEEE Transactions on Geoscience and Remote Sensing, **58**, 1587–1597, doi: 10.1109/TGRS.2019.2947085.

Wapenaar, C. P. A., and A. J. Berkhout, 1989, Elastic wave field extrapolation: Redatuming of single- and multi-component seismic data: Elsevier.

Ziolkowski, A., G. Parkes, L. Hatton, and T. Haughland, 1986, The signature of an air gun sarray: Computation from near-field measurements including interactions: Geophysics, **47**, 1413–1421, doi: 10.1190/1.1441289.

Biographies and photographs of the authors are not available.